Electronic Supplementary Material (ESI) for Lab on a Chip.

Supplementary Information for:

Graphene-Based Microfluidics for Serial Crystallography

Shuo Sui,[a] Yuxi Wang,[a] Kristopher W. Kolewe,[a] Vukica Srajer,[b] Robert Henning,[b] Jessica D. Schiffman,[a] Christos Dimitrakopoulos,[a] and Sarah L. Perry*[a]

[a] Department of Chemical Engineering, University of Massachusetts Amherst, Amherst, MA 01003, USA
[b] Center for Advanced Radiation Sources, University of Chicago, Argonne, IL 60439, USA
*Correspondence email: perrys@engin.umass.edu

S1. X-ray Compatibility

In designing an X-ray transparent microfluidic device for use in protein crystallography three main considerations with respect to the interaction between materials and X-rays must be taken into account: (i) attenuation and (ii) scattering of X-rays passing through device materials, and (iii) the strength of the diffraction resulting from a crystal. Attenuation results from the absorption of photons into the material, thereby decreasing the intensity of both the incident X-ray beam and the resultant signal. Scattering is an elastic redirection of photons based on the internal structure of the material and can affect the signal-to- noise. The strength of the diffraction signal from a crystal is related to not only the degree of order within the crystal, but also the packing density and size of the crystal.[1,2]

Attenuation can be calculated for a particular energy based on the exponential decay in intensity of a narrow beam of monochromatic photons from an incident intensity I_0 as it passes through a material of thickness x with a linear attenuation coefficient of the material μ.[3,4]

$$I = I_0 \exp(-\mu x) \tag{S1}$$

Attenuation coefficients have been well studied and documented for elemental materials.[3] For a compound containing multiple elements, a linear attenuation coefficient can be calculated based on the sum of the contribution to attenuation from each of the individual elements i, weighted based on their mass fraction w_i.

$$\mu = \sum \mu_i w_i \tag{S2}$$

Table S1 lists the chemical and atomic mass fractional compositions of various materials commonly used in microfluidic device manufacture. Calculated values for the linear attenuation coefficient for SiO_2, Si_3N_4, PDMS, COC, PMMA, graphene, and PDA can then be graphed as a function of either photon energy (Figure S1a) or X-ray wavelength (Figure S1b). As can be seen, the attenuation coefficient varies significantly as a function of photon energy. Soft X-rays (lower energy) attenuate much more strongly than do harder X-rays (higher energy), thus the energy of X-rays used for an experiment can have a significant effect on the signal observed from a device.

Table S1. Atomic mass fraction, density, and a calculated value for the linear attenuation coefficient μ at 1Å (12.4 keV) for various materials used in microfluidic devices.[4-8]

Element	Air	Quartz SiO_2	PDMS $Si_{61}O_{60}C_{124}H_{368}$	Silicon Nitride Si_3N_4	COC C_9H_{14}	PMMA C_5H_8O	Graphene C	PDA $C_8H_5NO_2$
H	--	--	0.08182	--	0.11546	0.09586	--	0.03552
C	0.00015	--	0.32853	--	0.88454	0.71394	1.00000	0.67623
N	0.75518	--	--	0.39938	--	--	--	0.09857
O	0.23179	0.53257	0.21175	--	--	0.19020	--	0.22520
Si	0.01288	0.46743	0.37791	0.60062	--	--	--	--
Density (g/cm^3)	0.001225	2.65	0.92	3.2	1.02	0.94	1.80	1.03
μ at 1Å (cm^{-1})	0.00291	50.7	39.5	10.8	5.80	7.82	6.51	8.87

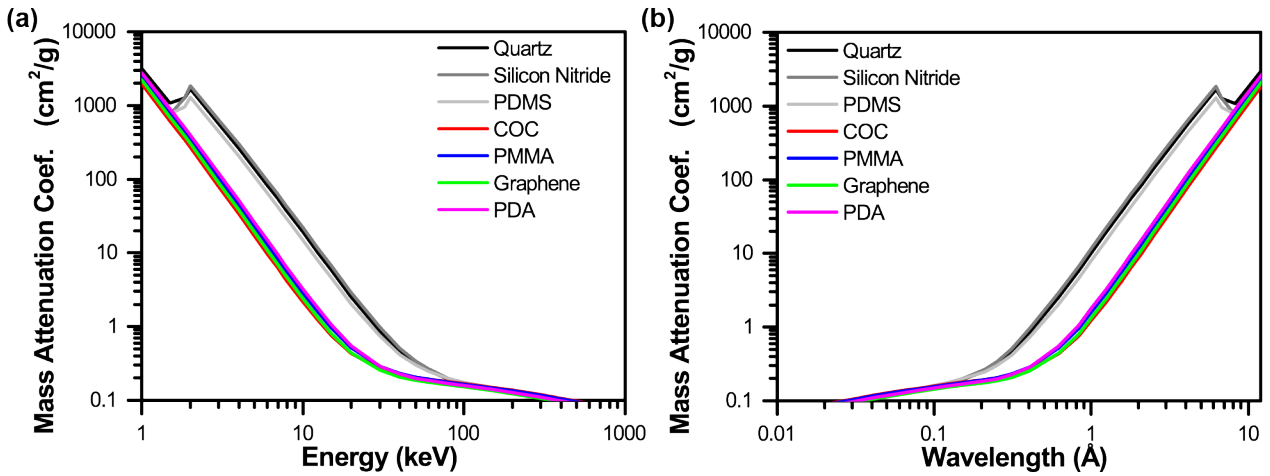

Figure S1. Linear attenuation coefficients μ for quartz, silicon nitride, PDMS, COC, PMMA, graphene, and PDA as a function of X-ray **(a)** energy or **(b)** wavelength.

Using values for the attenuation coefficient, the transmission factor I/I_0 can then be calculated as a function of material thickness. A plot of I/I_0 vs. film thickness at a photon energy of 12.4 keV, or a wavelength of 1Å, is shown in Figure S2a, comparing the attenuation effects of silicon-rich materials such as PDMS and lower atomic number organic thin films like COC and PMMA. As an be seen in Figure S2b, the difference in X-ray attenuation comparing the various films becomes increasingly significant with increasing film thickness. These calculations can be extended for typical microfluidic device architectures at different X-ray energies (Figure S2c-f). Here, differences in both the atomic number content and the overall device thickness comparing our graphene-based microfluidic device architectures (Figure S2c,d) with our previously-reported PDMS-COC (Figure S2e,f) devices demonstrates the tremendous decrease in the overall loss of signal from our devices, and suggests the potential for significantly higher signal-to-noise.

Several interesting observations can be made from the data presented in Table S1 and Figure S1. PDMS and PMMA have very similar densities; however the linear attenuation coefficient for PDMS is significantly higher. This difference arises from the silicon content in PDMS. Heavier atoms present a larger cross-section for interacting with photons and will thus cause a larger degree of attenuation. The density of a material also plays a role in the degree of attenuation observed, with higher density materials increasing the number of atoms which can interact with a photon for a given path length, though this effect is less significant than elemental composition.

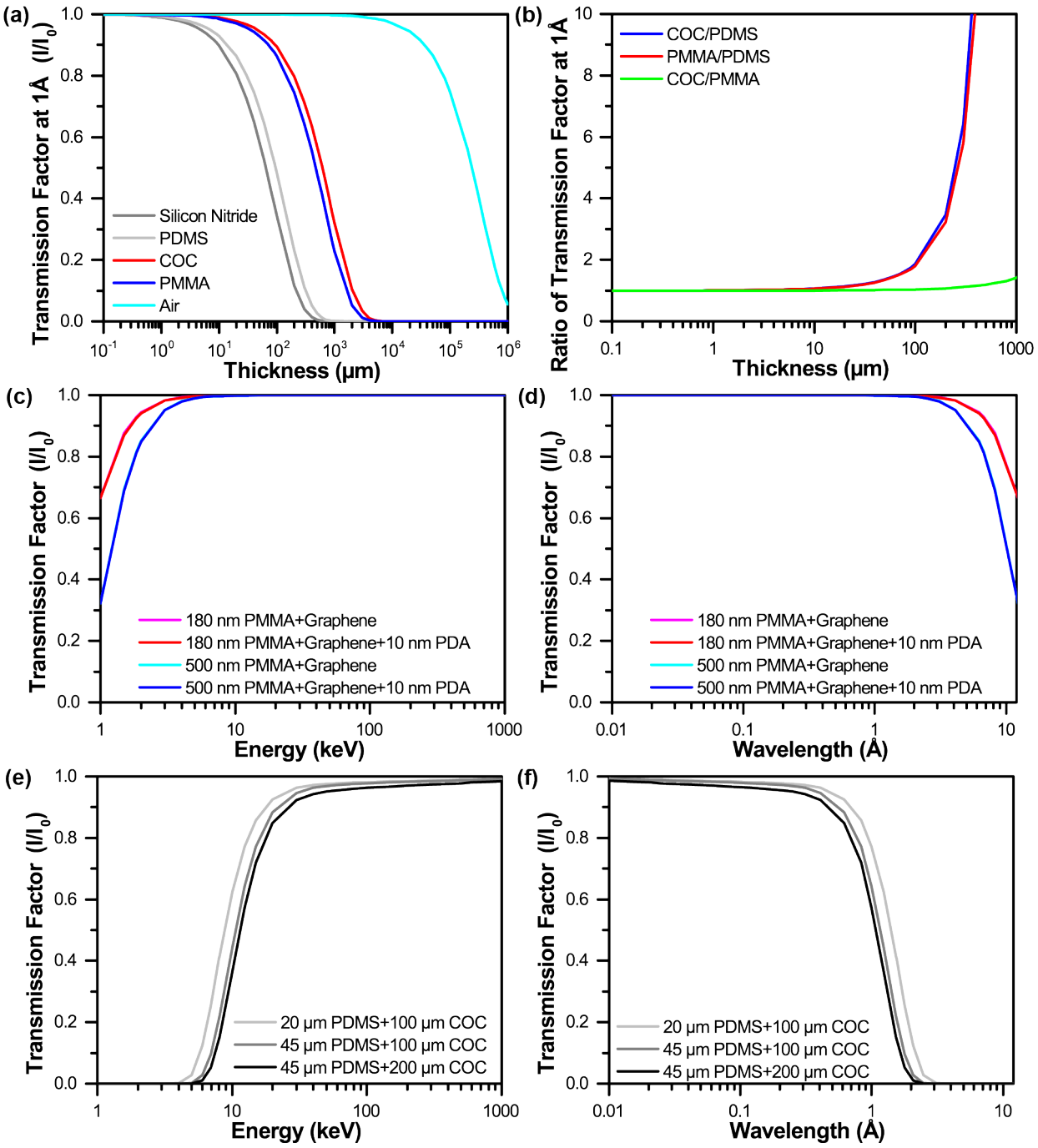

Figure S2. (a) A comparison of the transmission factors I/I_0 for varying thicknesses of silicon nitride, PDMS, COC, and PMMA at a photon energy of 12.4 keV, or a wavelength of 1Å. **(b)** Quantification of the ratio of transmission factors I/I_0 at 1Å between COC/PDMS, PMMA/PDMS, and COC/PMMA.A comparison between the transmission factors I/I_0 for various graphene-PMMA-PDA architectures **(c,d)** and previously-reported X-ray compatible PDMS-COC device architectures[9-15] **(e,f)** and as a function of X-ray energy **(c,e)** or wavelength **(d,f)**.

Knowing the attenuation coefficient for various materials, an expression for the attenuation through a series of different films j can be calculated based on Eq. (S1).

$$I = I_0 \exp\left(-\sum \mu_j x_j\right) \tag{S3}$$

In Figure S2c-f, we compare the transmission factor as a function of X-ray energy (or wavelength) for different graphene-based devices tested here, and PDMS-based device geometries reported previously.[9-15] At an X-ray energy of approximately 12.4 keV (1Å), transmission through the PDMS-based devices was in the range of 57-77%. This level of signal transmission was sufficient to enable the collection of high quality X-ray data from relatively large crystals. However, the 99.9% signal transmission from our ultra-thin graphene-based devices will enable data collection from microcrystals. To achieve a similar level of signal transmission from ultra-thin, microfabricated silicon nitride windows would require a thickness of 100 nm. While windows of this thickness have been reported successfully,[16-18] such devices cannot be manufactured with the same ease and low cost as soft lithographic and replica molding-based approaches.

S2. Background Scattering and Signal-to-Noise

In addition to attenuation, background scatter from the device materials can adversely affect the resultant signal-to-noise. Scattering is a result of the internal structure of a material. Thus the characteristic length-scale of this internal geometry defines the location of this scattering signal. For instance, scattering rings resulting from a relatively thick layer of COC can be clearly observed above the overall envelope shape of the amorphous background (Figure S3a,b).[1,2,9-15,19] The intensity of these background scattering signals scales in a roughly linear fashion with sample thickness.

Because crystallography experiments commonly involve sample rotation, variations in path length as a function of the incident angle also need to be taken into account. The effect of incident angle on the apparent path length (relative to the minimum path length achieved when the chip is mounted perpendicular to the X-ray beam at ϕ = 0°) is described by: (Figure S4).

$$path\ length = \frac{1}{\cos(\phi)} \qquad \text{(S4)}$$

However, the observed levels of background scatter are only relevant when compared to the strength of the diffraction signal from a crystal of interest. In this sense, while the overall level of background scattering could ultimately swamp the entire diffraction signal, the challenge with material-specific scattering rings is the potential for the loss of data over a particular range of resolution or q-space. Our goal, in developing ultra-thin graphene-based microfluidics is to enable the collection of X-ray diffraction data from either tiny, or weakly diffracting crystals to enable serial crystallography. In Figure S5, we compare the observed signal-to-noise in our previously-reported COC/PDMS-based devices,[3,4,9-15] compared with the PMMA/graphene-based devices reported here. Both the 2D diffraction images and the integrated 1D intensities clearly demonstrate the significant loss in signal-to-noise resulting from the COC scattering ring. This challenge was eliminated in our PMMA/graphene-based devices by decreasing the overall thickness of the polymeric layer by approximately two orders of magnitude. It should be noted that the data presented in Figures 6 and S5 is the result of integration in 2θ across the entire image, rather than along a line. Thus, the presence of multiple diffraction peaks at nearly the same resolution could result in apparent broadening of the integrated signal. All images were well exposed, typically with several saturated diffraction spots (~65,000 counts).

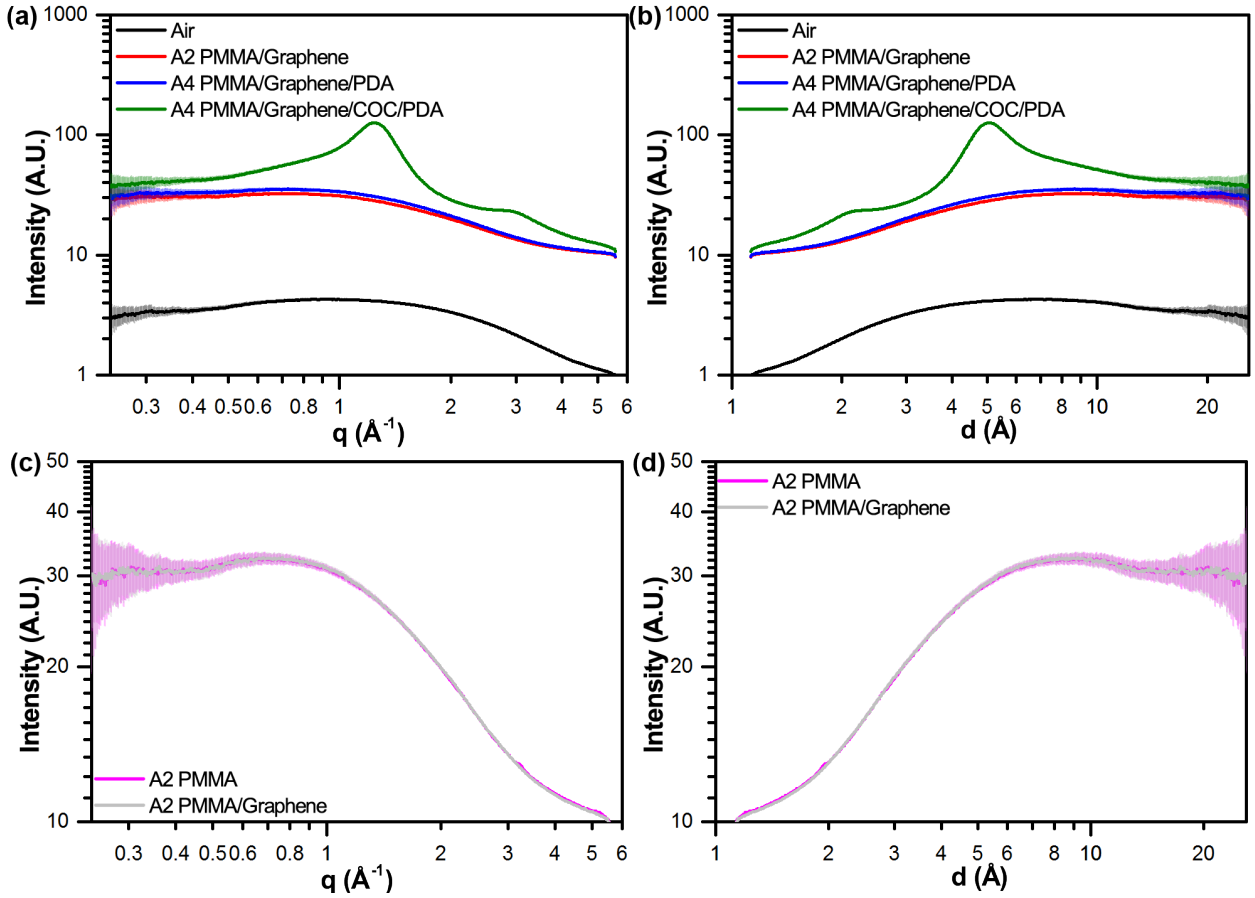

Figure S3. One-dimensional integrated X-ray intensity profiles showing the background scatter resulting from various device geometries. (**a,b**) A comparison of the level of background scattering resulting from a 1.5 μs polychromatic X-ray pulse train interacting with the air background, as well as varying thicknesses of PMMA with graphene, PDA surface treatment, and a 100 μm COC layer as a function of q-space **(a)** or d-spacing **(b)**. While the presence of thin polymeric films does increase the overall signal, the impact of either 180 nm A2 or 500 nm A4 PMMA is significantly lower than the larger signal resulting from 100 μm COC. The improvements in signal are due in part to the decrease in overall thickness, as well as the absence of the characteristic scattering bands observed for COC (green), above the overall shape of the amorphous background. A similar comparison is given in **(c,d)** showing the negligible effect of a single layer of graphene on a 180 nm A2 PMMA film.

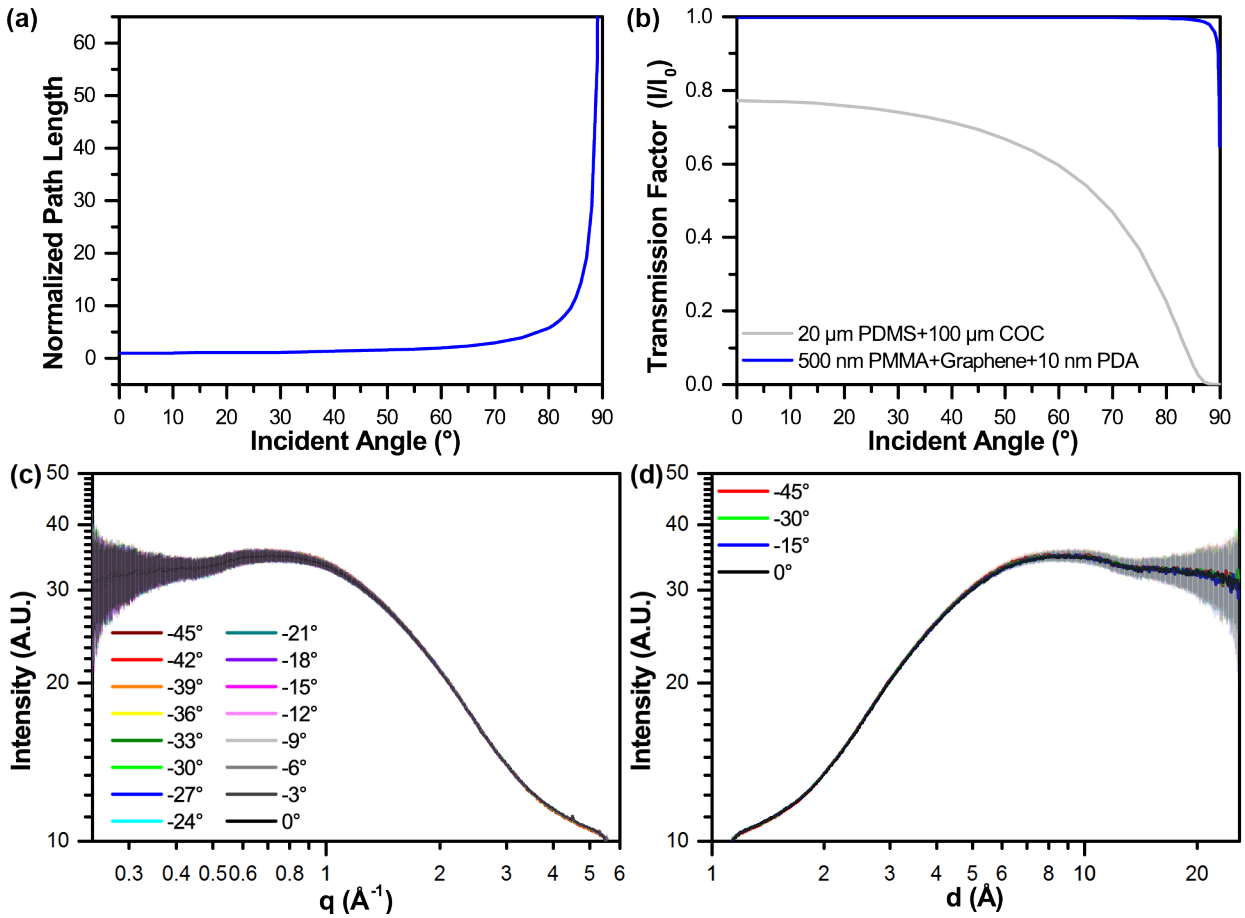

Figure S4. **(a)** Normalized path length as a function of incident angle, calculated using Eq. (S4). **(b)** A comparison of the transmission factors I/I_0 for a typical COC/PDMS-based and a PMMA/graphene-based device. **(c)** One-dimensional integrated X-ray intensity profiles showing the effect of incident angle on the background signal resulting from an empty 500 nm PMMA/graphene/PDA device as a function of q-space. **(d)** A subset of the data from **(c)**, plotted as a function of resolution, or d-spacing.

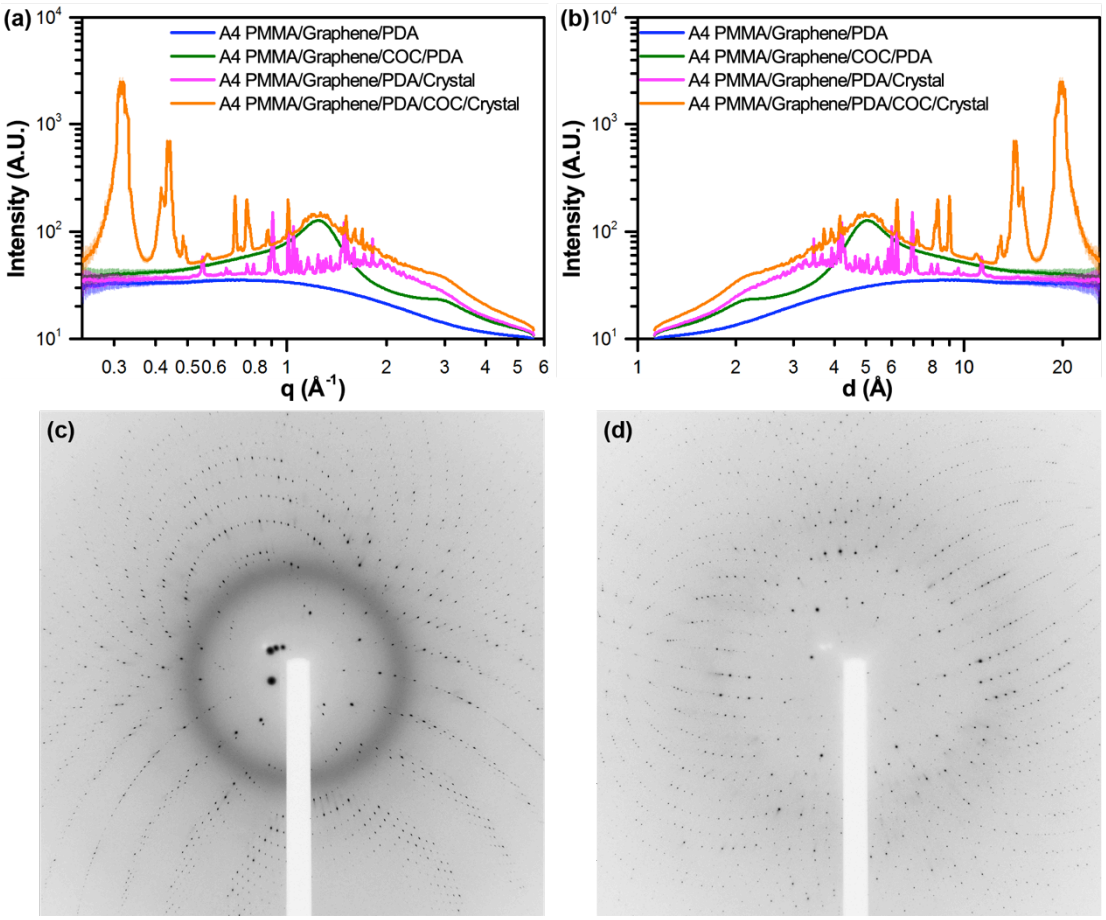

Figure S5. One-dimensional integrated X-ray intensity profiles showing the relative strength of the observed diffraction signal from a HEWL crystal compared to the noise resulting from background scattering due to the presence of device materials as a function of q-space **(a)** or d-spacing **(b)**. A significant decrease in signal-to-noise is observed in the regions where significant scattering results from a 100 µm COC layer. The corresponding two-dimensional diffraction images for the **(c)** A4 PMMA/Graphene/PDA/COC/Crystal dataset (orange), and the **(d)** A4 PMMA/Graphene/PDA/Crystal dataset (magenta) shown in **(a)** and **(b)**.

S3. Film Permeability Tests

One of the most significant challenges in decreasing the overall thickness of the microfluidic device architecture was the need to avoid evaporative losses from the device over time. Most protein crystallization experiments require days or weeks to allow for crystal growth. While the devices could be stabilized in a controlled humidity environment during this time, the challenge of device stability during transportation and data collection remains. However, our goal is to create a microfluidic device architecture that can enable a stable, stand-alone environment for a period of weeks or months. This would allow for microfluidic crystallization approaches to better mimic current well plate-based technologies, and facilitate translation to a broader audience of users. To quantify the loss of water through our device materials as a function of time, we used our films, attached to an adhesive polyester film with an opening cut to match the well plate structure as a mimic of our device geometry. These films were then sealed over the wells via vacuum grease, to isolate 300 µL of a solution of red food dye in water in a 96-well plate. All samples were performed in triplicate. The absorbance of the colored solutions was then monitored at 300 nm and 450 nm using a plate reader as a function of time. The results in Figure S6 (and Figure 5) clearly show the evaporative loss of water from the open-well control samples after a period of 48 hours. The presence of a PMMA film delayed this process, with some improvement observed with

increasing film thickness. However, the addition of a single layer of graphene as a diffusion barrier was able to prevent the loss of water and stabilize the samples for more than two weeks. Similar results were obtained with a 100 µm-thick film of COC, which was expected to show low water permeability.[3,5] These experiments also demonstrate that lateral diffusion of water between layers is not a significant concern for our device architecture.

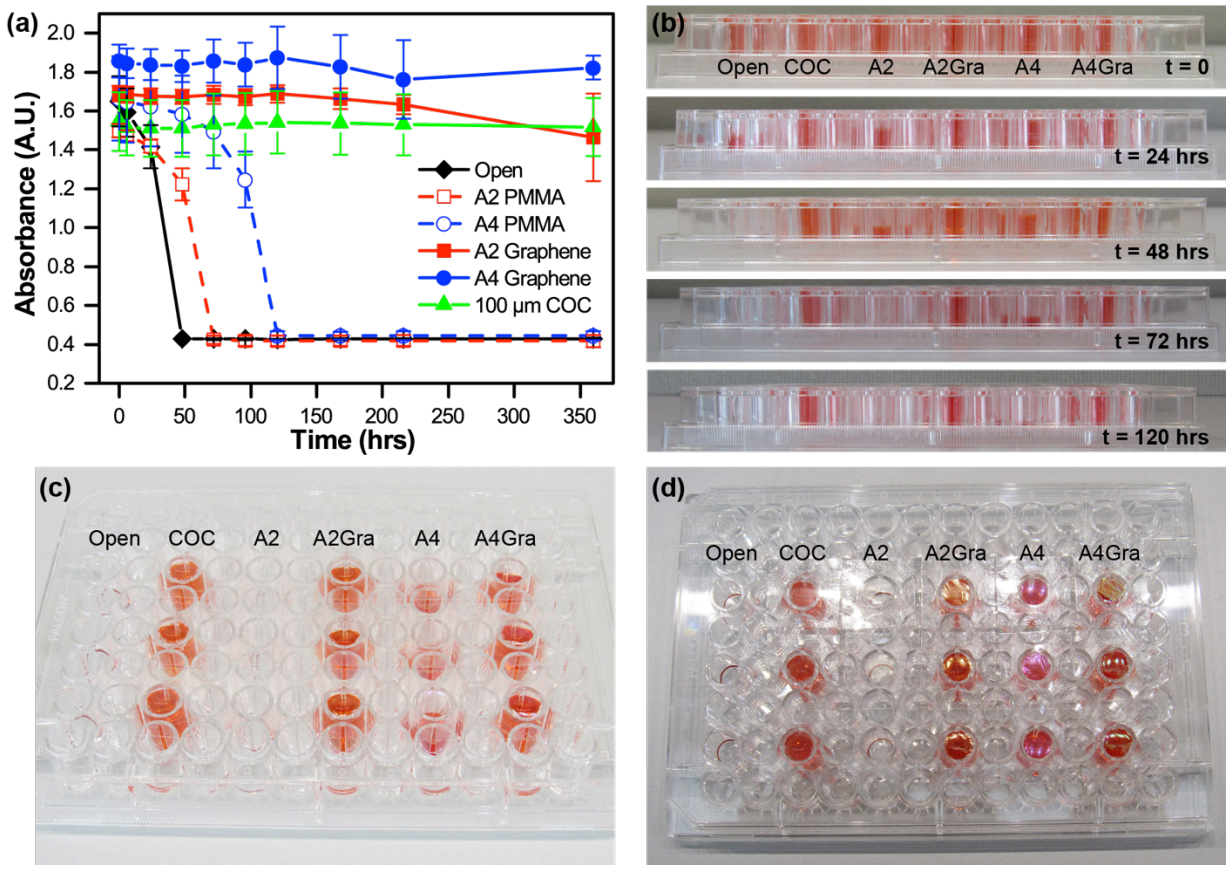

Figure S6. **(a)** Measurement of the absorbance of colored solutions as a function of time at 300 nm, demonstrating the water permeability of various PMMA, PMMA/graphene, and COC films. Both the thicker 100 µm COC film, and the two PMMA/graphene films show no significant decrease in signal over the course of more than two weeks. **(b)** Photographs of the experimental setup showing changes in the liquid levels as seen by a side-view. Perspective **(c)** and top-view **(d)** images of the well plate after 72 hours, showing the complete evaporation of water from both the open and the A2 PMMA (~180 nm) wells, and the partial evaporation of water from the A4 well (~500 nm). In **(d)**, the iridescent sheen of the graphene film can be seen on both the A2Gra and A4Gra wells.

Additional permeability experiments were performed directly in microfluidic devices, again using colored solutions for visualization purposes. A comparison was run for devices stored under ambient laboratory conditions and chips stored in sealed petri dishes containing 200 µL of water and 4°C to create a humidified environment. Both the microbatch and the counter-diffusion device architectures were investigated (Figure S7). Visual inspection of microbatch devices (Figure S7a) devices indicate no significant water loss over the course of 96 hours, regardless of storage conditions. It is interesting to observe differences in the timing and growth of lysozyme crystals from these solutions, which we attribute to temperature-related differences in protein solubility.

While microbatch trials indicated a very stable sample environment, more significant water permeation was observed from the counter-diffusion device geometry (Figure S7b). Following incubation at ambient laboratory conditions, significant water loss was observed from the counter-diffusion chip over the course of only 8 hours,

with complete evaporation of the ~2 µL sample volume observed between 1-2 days. Interestingly, incubation at 4°C in a humidified environment alleviated this issue, and produced stable samples for more than 6 days. We hypothesize that the stable microbatch sample environment is due to complete coverage of the sample chamber by PMMA/graphene films. However, for the counter-diffusion chips used here, graphene windows only covered the large sample chamber, rather than the entirety of the device. Future device designs will address this issue.

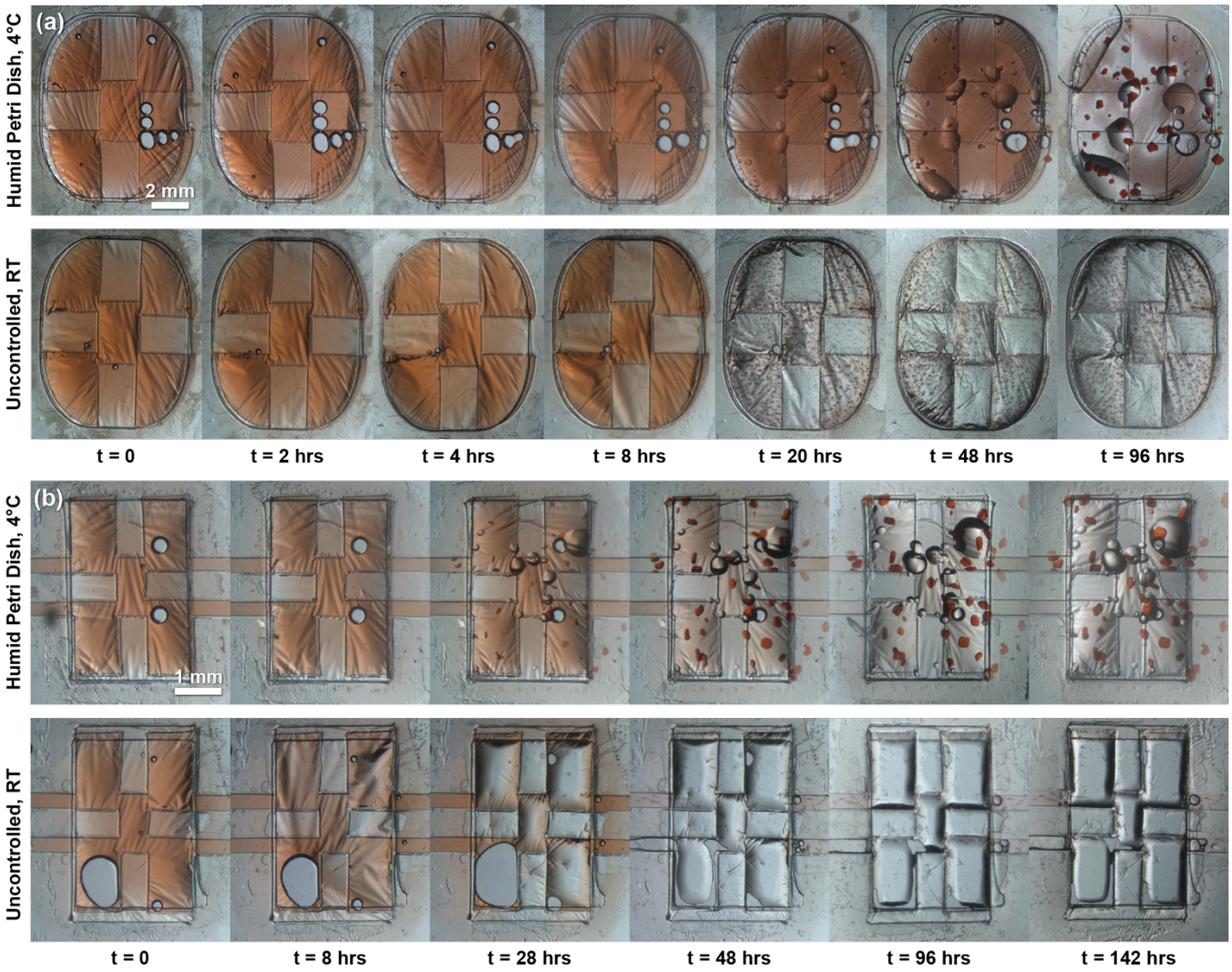

Figure S7. Optical micrographs showing the change in solution content within **(a)** microbatch and **(b)** counter-diffusion style microfluidic devices as a function of time. Devices were stored either in a sealed petri dish along with 200 µL of water at 4°C to create a hydrated environment, or under ambient laboratory conditions at room temperature. The filling solution consists of a lysozyme crystallization trial colored with red food coloring for improved visualization. For the devices stored in a humidified environment, droplets of condensation can be observed on the device, along with the formation of red-colored lysozyme crystals. In the microbatch experiment in **(a)**, no significant changes in solution content were observed over the course of the experiment, regardless of incubation conditions. Similar results were obtained in **(b)** for the counter-diffusion chip stored in a humidified environment. However, significant water loss was observed over the course of 8 hours for the counter-diffusion chip incubated at ambient conditions.

S4. Device Fabrication

The overall chip architecture consists of five layers, which allow for various different functional layouts (Figure 2 and Figure S8). The fluidic channels of the device are defined by a 100-µm thick cyclic olefin copolymer (COC, Topas, 6013) film, although this could be easily substituted for an alternative material and/or thickness film. This

spacer layer defines the overall thickness of the device. The overall device structure was cut into the spacer film using a cutting plotter (Graphtec CE6000). In our microbatch-style devices, this structure consisted simply of a cut-out circle, whereas for a counter-diffusion architecture, a more complex channel geometry was utilized (Figure 2 and Figures S8, S9). For both of these structures, care was taken to include support structures to prevent collapse of the thin PMMA/graphene film. These can be seen as small tabs of COC that extend into the large crystallization chamber for both microbatch and counter-diffusion, and the thin strip of material bifurcating the inlet channels in the counter-diffusion chip (Figures 2 and 3).

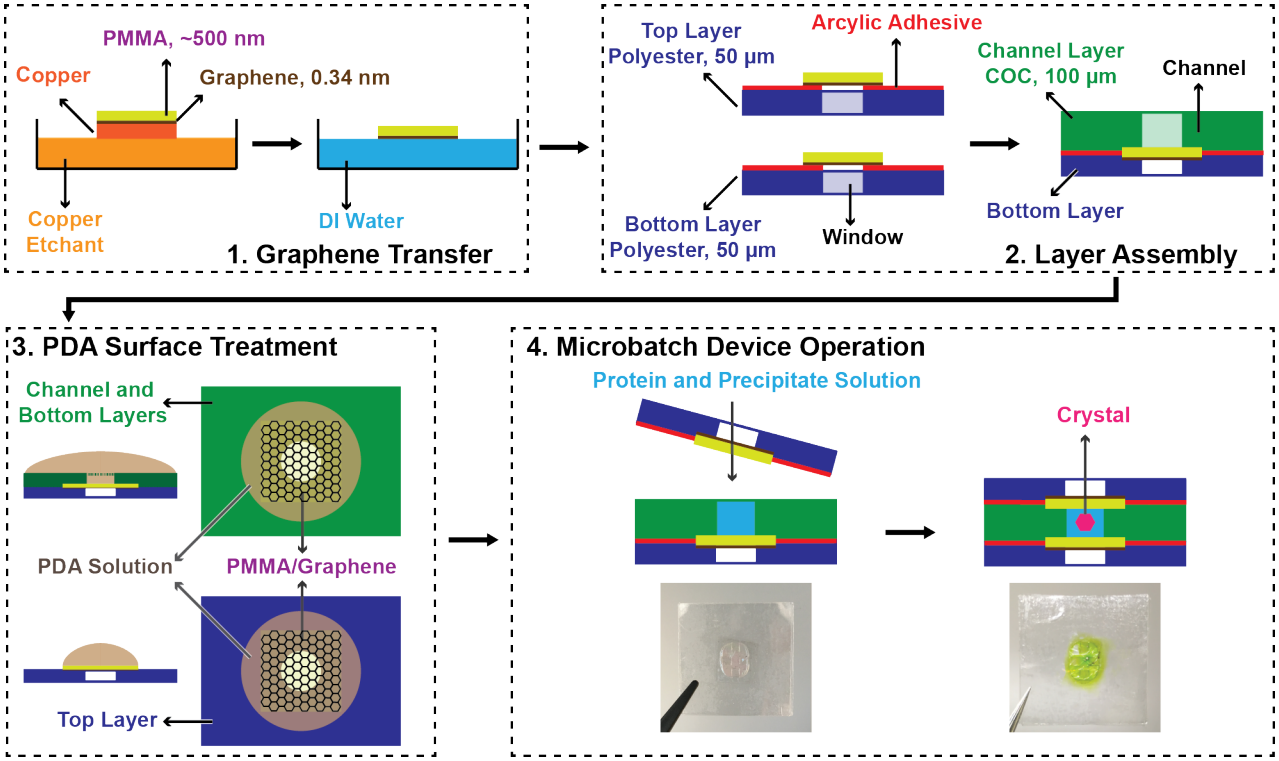

Figure S8. Schematic depiction of the fabrication scheme for thin-film, microbatch-style, graphene-based microfluidics. **(1)** Firstly, CVD-grown graphene on copper is first coated with a layer of PMMA, followed by etch-releasing from the copper substrate. The subsequent film is floated on the surface of water for **(2)** transfer to an adhesive polyester support layer to define the window areas of the device. This layer is then adhered to a COC layer containing the cut-out pattern for the well. **(3)** A hydrophilic PDA surface treatment of both the top PMMA/graphene film and the bottom layer containing the crystallization chamber facilitates easy wetting of the final device. **(4)** The final, assembled device is held together by the adhesive layers defining the window structures, leaving the PMMA/graphene window areas free of excess material. Microbatch trials can be set up by the addition of protein and precipitant solutions prior to sealing the device. Photographs of an empty and a filled device (green food coloring used for visualization purposes) are also shown.

The microfluidic channels and/or chambers were then sealed on one side with a PMMA/graphene film, supported by an adhesive-backed polyester film (McMaster Carr) with cut-out features to define fluidic inlets and/or window areas, as necessary (Figures 2,3 and †ESI Figure S8). Here, the backing layer provides additional structural stability, while helping to define inlets, and providing a facile way to adhere the various layers together. Following assembly of the COC fluidic layer to the adhesive bottom layer containing a PMMA/graphene film, both the top and bottom halves of the device were coated with poly(dopamine) (PDA) to create a hydrophilic surface and facilitate channel wetting, before final device assembly and use (Figure 2 and Figures S8, S9).[20,21]

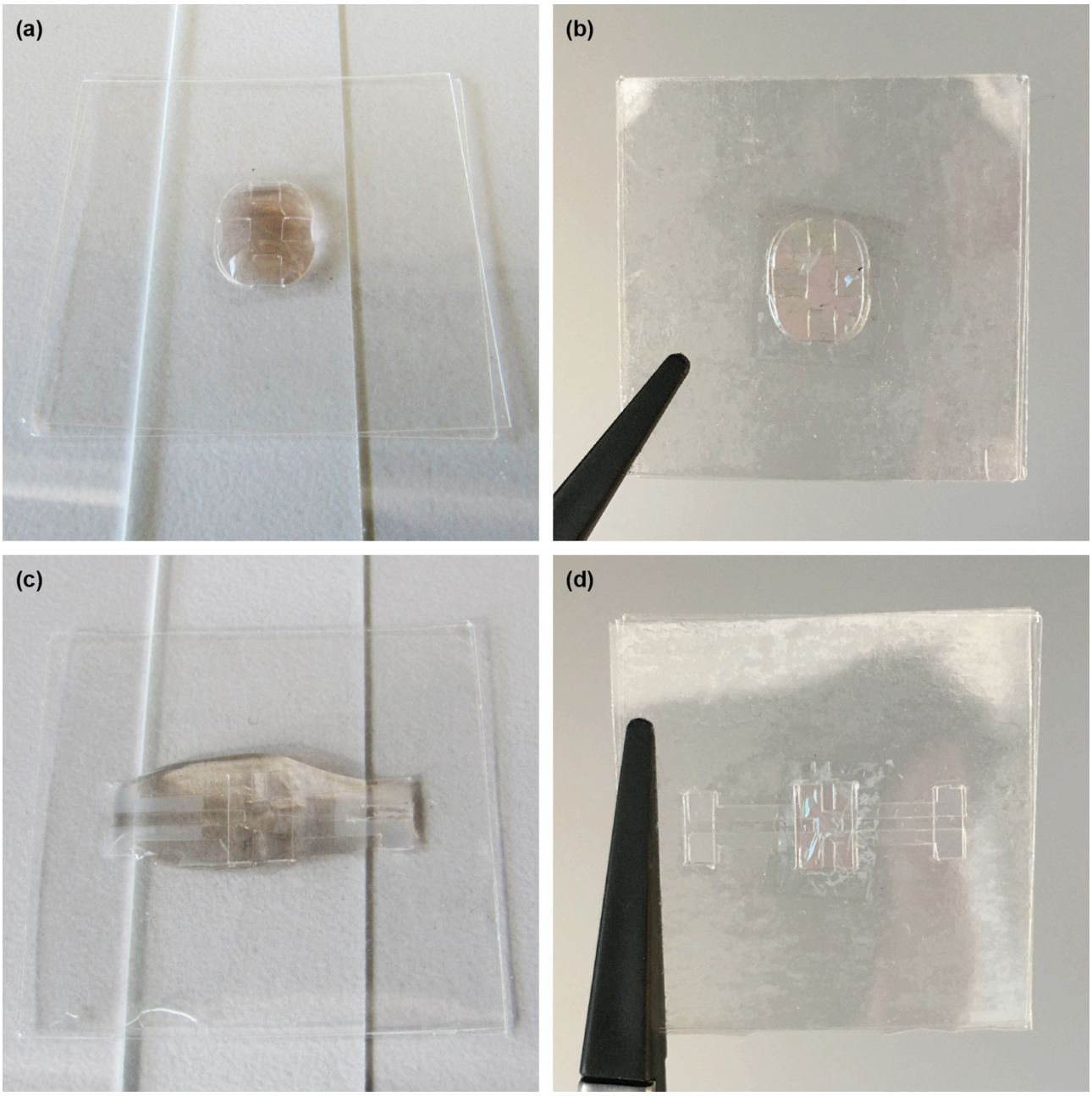

Figure S9. Photographs of **(a)** a microbatch chip undergoing PDA treatment, **(b)** the final, assembled device, **(c)** a counter-diffusion style chip undergoing PDA treatment, and **(d)** the final device.

S5. Atomic Force Microscopy (AFM)

We utilized atomic force microscopy (AFM) to characterize the surface roughness of our various films. Surface scans of PMMA/graphene and PDA coated PMMA/graphene were acquired using the Cypher ES atomic force microscope (Asylum Research, Santa Barbara CA).[4-8,22] Samples were imaged in AC mode with Tap-300G cantilevers (Budget Sensors). The PMMA/graphene films showed a very smooth surface, with a level of roughness characteristic of the original copper substrate from CVD graphene synthesis (Figure S10a). The deposition of PDA onto PMMA had minimal effect on surface roughness although PDA aggregation was slightly larger on thicker PMMA surfaces, where isolated aggregates were observed up to a size of 0.5 μm (Figure S10b,c).

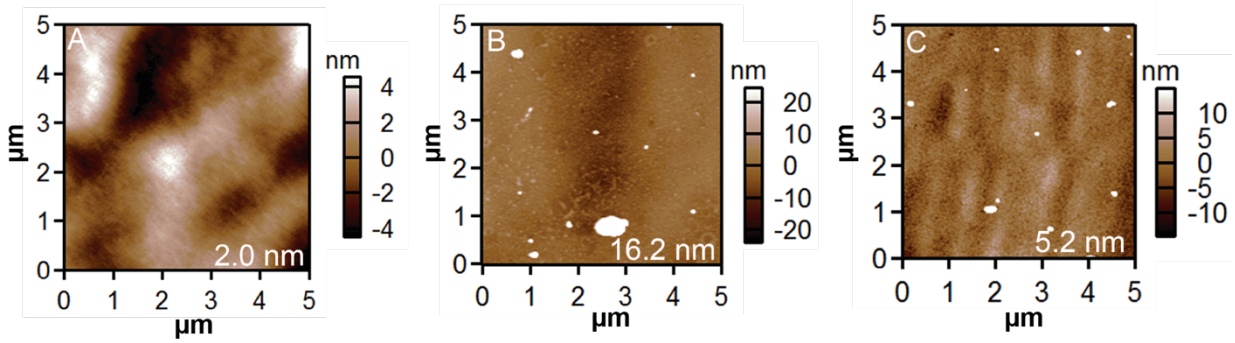

Figure S10. AFM topography micrographs of **(a)** 500 nm PMMA on graphene, **(b)** 500 nm PMMA coated with PDA on graphene, and **(c)** 180 nm PMMA coated with PDA on graphene. Deposition of PDA onto PMMA had minimal effect on surface roughness although PDA aggregation was slightly larger on thicker PMMA surfaces with isolated aggregates up to 0.5 µm.

S5. Contact Angle Measurements

A PMMA/graphene film was transferred from the aqueous rinse solution onto a silicon wafer (graphene-side down) and allowed to air dry 3 hours to facilitate strong binding between the film and the wafer surface. A PDA treatment was then applied to the PMMA film. The contact angle of both a treated and an untreated PMMA/graphene film were measured using goniometry with MilliQ water (Ramé-Hart). The untreated PMMA film showed a contact angle of 74° (Figure S11a). Following a 5 hour PDA treatment, this contact angle dropped to 36° (Figure S11b), easily facilitating capillary-driven flow into our microfluidic channels.

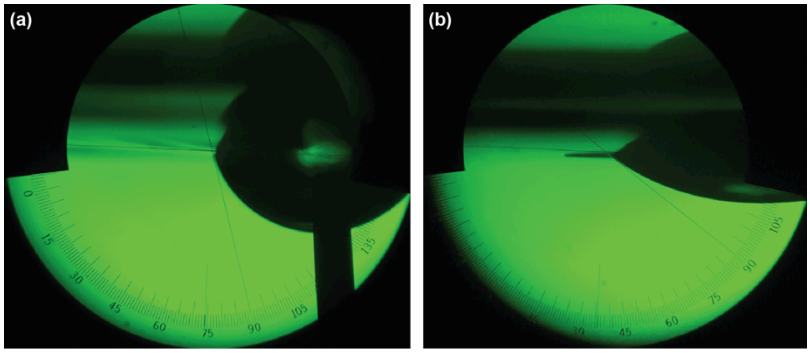

Figure S11. Optical micrographs of contact angle measurements for **(a)** an untreated 500 nm PMMA on graphene, and **(b)** 500 nm PMMA/graphene, following a 5 hour PDA treatment.

S6. Protein Crystallography

Data collection was performed in polychromatic mode 12 keV (1.03 Å, 5% bandwidth) on the 14-ID-B beamline at the Advanced Photon Source at Argonne National Laboratory.[9-15,23] Data were collected in a pseudo-serial fashion using a 1.5 µs exposure from a micro-focused polychromatic X-ray beam (spot size of 35 x 35 μm^2, FWHM), and the storage ring operating in 24-bunch mode (11 consecutive X-ray pulses of 100 ps duration). A Rayonix MX340-HS detector was used, with a sample-to-detector distance of 175 mm. The microfluidic chips were mounted directly on the φ spindle of the goniometer using a modified magnetic mount (Hampton Research; Figure 3a). Data were typically collected at 3° intervals over the range of -45° and 45°. This spacing was chosen to enable optimal coverage of diffraction space given the bandwidth of the beamline at 12 keV.

The crystals grown in our PMMA/graphene devices were large enough to enable the collection of data from multiple different independent locations. We first determined the usable lifetime of our crystals by attempting to

collect an 90° dataset for our tetragonal HEWL crystals (31 frames total, 3° intervals from -45° and 45°).[9-15,24] We observed a significant decrease in resolution, along with a significant increase in sample mosaicity, as evidenced by radial streaking of diffraction spots, after only 16 exposures. Moving forward, we chose to collect only 3-4 frames of data from an individual location, so as to minimize the effects of radiation damage, while allowing for collection of a complete dataset.

Table S2. Crystallographic statistics for data obtained using on-chip micro-diffraction Laue analysis of various HEWL crystals. Values in parentheses are for the highest integrated resolution shell.

Parameter	Microbatch PMMA/Graphene	Microbatch PMMA/Graphene	Microbatch PMMA/Graphene/COC	Counter-Diffusion PMMA/Graphene
Data Collection				
Total # Frames	55	32	59	30
# Frames/Spot	3	4	4	3
Resolution (Å)	50-1.40	50-1.41	50-1.41	50-1.46
Space Group	$P4_32_12$	$P4_32_12$	$P4_32_12$	$P4_32_12$
Unit Cell Dimensions (Å)	a=b=79.1, c=37.7	a=b=79.1, c=37.6	a=b=79.1, c=37.3	a=b=79.1, c=37.8
Single Reflections				
Total Observations	150,678	90,828	143,638	70,996
Unique Observations	18,294	15,991	17,608	15,629
Redundancy	8.2	5.7	8.2	4.5
R_{merge} **on** F^2	0.054	0.049	0.077	0.047
R_{merge} **on** F	0.036	0.032	0.049	0.031
$<F/\sigma(F)>$	63.9 (28.6)	62.0 (41.9)	50.7 (19.9)	60.4 (33.4)
Single and Multiple Reflections Combined				
Completeness (%)	77.2 (25.1)	69.4 (26.7)	76.6 (28.4)	74.8 (27.1)
Structure Refinement				
R_{work}	0.149	0.145	0.156	0.145
R_{free}	0.163	0.166	0.176	0.167
Ramachandran Statistics				
Favored Residues	123 (96.9%)	123 (96.9%)	122 (96.1%)	122 (96.1%)
Allowed Residues	4 (3.1%)	4 (3.1%)	5 (3.9%)	5 (3.9%)
Disallowed Residues	0 (0.0%)	0 (0.0%)	0 (0.0%)	0 (0.0%)

We collected data on three separate crystals grown in the same microbatch-style device. Two of the microbatch-grown crystals were located between the PMMA/graphene window structures, while the third grew opportunistically under the COC spacer. This provided us with the opportunity to directly compare differences in the quality of diffraction data achievable with our ultra-thin device geometry, with thicker X-ray compatible device designs (Table S2). All samples showed excellent signal-to-noise and values for R_{merge}, R_{work}, and R_{free}. Interestingly, we did not observed a significant decrease in resolution for the crystal present under the thicker COC film. This result may be due to the relatively strong diffraction signals expected from our large crystals. High quality crystallographic statistics were observed for all samples; however, the presence of the thick COC film did correspond with an increase in the values for R_{merge}, and a decrease in signal-to-noise, characterized by $<F/\sigma(F)>$. We defined our resolution cutoff as the point where completeness in the highest resolution shell dropped below 25%, provided that $<F/\sigma(F)>$ was greater than 3.0. The difference in criteria for determination of a resolution

cutoff for Laue data, as compared to monochromatic data, is related to the polychromatic nature of the diffraction, which results in a less abrupt loss of signal at the resolution edge. Figure S12 shows a plot of completeness vs. resolution for each of the datasets shown in Table S2. This plot demonstrates the high levels of completeness present over much of the resolution range, and the gradual loss of completeness at high resolution. Thus, while the reported statistics in Table S2 have the appearance of incompleteness, the lower average value of completeness over all hkls is merely a consequence of averaging and of the characteristics of Laue data.

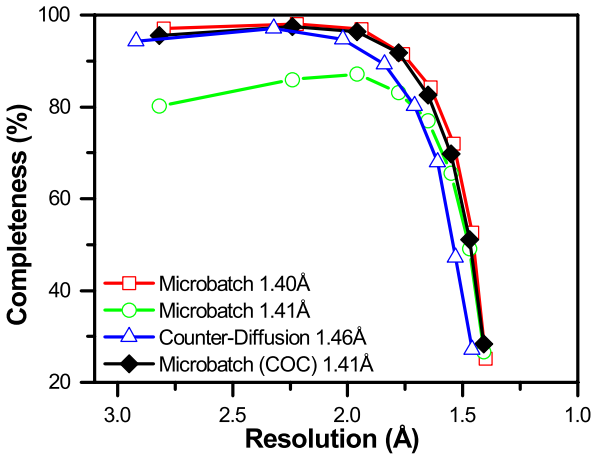

Figure S12. Graph of completeness vs. resolution for the four datasets shown in Table S2. The final resolution of the dataset is indicated in the legend.

The presence of a 100 μm-thick COC layer also had a significant effect on the observed signal-to-noise. An analysis of $<F/\sigma(F)>$ as a function of resolution (Figure 7) demonstrated that data collected through a more attenuating material, and the presence of increased background scatter, have a negative effect on the overall sensitivity of the measurement. This decrease in signal-to-noise was observed despite similar levels of completeness and redundancy in the overall dataset, compared with data collected through PMMA/graphene windows. In particular, a significant decrease in $<F/\sigma(F)>$ is observed at a resolution of ~2.5Å. This corresponds with the location of the smaller of the scattering bands observed for COC in Figure S3b and S5b. The effect of the larger scattering band observed at ~5.0Å was not observable in this data, due to the range of resolutions over which the binned $<F/\sigma(F)>$ data were provided by the processing software.

In addition to the microbatch data, we also collected data from a crystal that was grown via counter-diffusion. Comparison of crystallographic statistics does not indicate any significant difference in the overall quality of results obtained for these two techniques, which is expected for HEWL. However, in general, the counter-diffusion method would be expected to result in more reproducible crystal growth, due to the precise control over concentration gradients, diffusion, and mixing afforded by microfluidic devices.[9-11,16-18] Examination of the electron density maps generated from these various datasets show similar levels of structural detail, as would be expected from data extending to ~1.40Å (Figure S13). The quality of the data allows for unambiguous interpretation of structural details, including side-chain conformations and the location of bound water molecules.

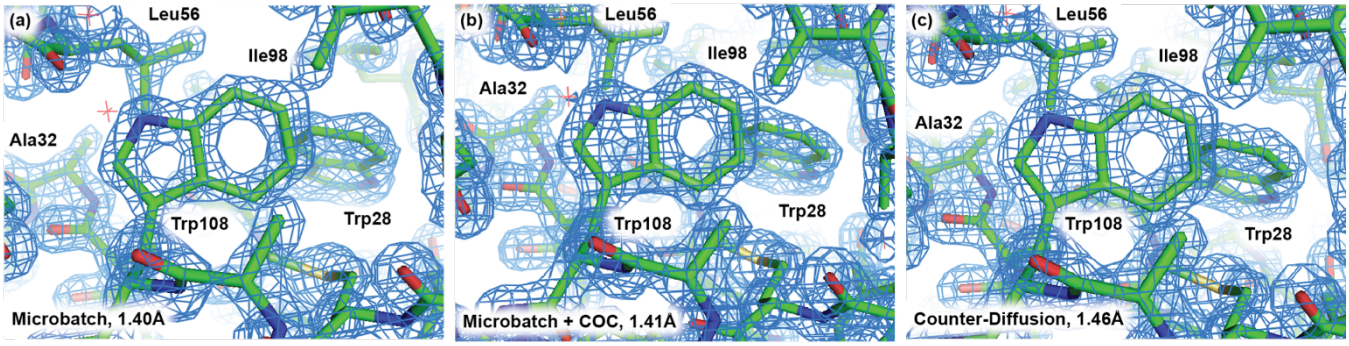

Figure S13. $2F_o–F_c$ electron density maps of HEWL grown in **(a)** microbatch to 1.40Å, **(b)** microbatch under a 100 µm COC film to 1.41Å, and **(c)** counter-diffusion to 1.46Å. Maps are contoured at 2σ and superimposed over a licorice representation of the protein structure surrounding Trp108.

References

1 J. L. Smith, R. F. Fischetti and M. Yamamoto, *Curr. Opin. Struct. Biol.*, 2012, **22**, 602–612.
2 J. M. Holton and K. A. Frankel, *Acta Crystallogr., Sect. D: Biol. Crystallogr.*, 2010, **66**, 393–408.
3 J. H. Hubbell and S. S. M, *Tables of X-ray Mass Attenuation Coefficients and Mass Energy-Absorption Coefficients from 1 keV to 20 MeV for Elements Z=1 to 92 and 48 Additional Substances of Dosimetric Interest*, National Institute of Standards and Technology, 1996.
4 E. D. Greaves and A. Manz, *Lab Chip*, 2005, **5**, 382–391.
5 P. S. Nunes, P. D. Ohlsson, O. Ordeig and J. P. Kutter, *Microfluid. Nanofluid.*, 2010, **9**, 145–161.
6 *CRC Handbook of Chemistry and Physics*, CRC Press, New York, 76 edn. 1996.
7 D. Chai, Z. Xie, Y. Wang, L. Liu and Y.-J. Yum, *ACS Appl. Mater. Interfaces*, 2014, **6**, 17974–17984.
8 *http://www.appliednanotech.net/tech/graphene_films.php*.
9 S. L. Perry, S. Guha, A. S. Pawate, A. Bhaskarla, V. Agarwal, S. K. Nair and P. J. A. Kenis, *Lab Chip*, 2013, **13**, 3183–3187.
10 S. Guha, S. L. Perry, A. S. Pawate and P. J. A. Kenis, *Sens. Actuators, B*, 2012, **174**, 1–9.
11 S. L. Perry, S. Guha, A. S. Pawate, R. Henning, I. Kosheleva, V. Srajer, P. J. A. Kenis and Z. Ren, *J. Appl. Cryst.*, 2014, **47**, 1975–1982.
12 A. S. Pawate, V. Srajer, J. Schieferstein, S. Guha, R. Henning, I. Kosheleva, M. Schmidt, Z. Ren, P. J. A. Kenis and S. L. Perry, *Acta Crystallogr., Sect. F: Struct. Biol. Commun.*, 2015, **71**, 823–830.
13 D. S. Khvostichenko, E. Kondrashkina, S. L. Perry, A. S. Pawate, K. Brister and P. J. A. Kenis, *Analyst*, 2013, **138**, 5384–5395.
14 D. S. Khvostichenko, J. M. Schieferstein, A. S. Pawate, P. D. Laible and P. J. A. Kenis, *Cryst. Growth Des.*, 2014, **14**, 4886–4890.
15 E. Kondrashkina, D. S. Khvostichenko, S. L. Perry, J. V. Osinski, P. J. A. Kenis and K. Brister, *J. Phys.: Conf. Ser.*, 2013, **425**, 012013.
16 M. S. Hunter, B. Segelke, M. Messerschmidt, G. J. Williams, N. A. Zatsepin, A. Barty, W. H. Benner, D. B. Carlson, M. Coleman, A. Graf, S. P. Hau-Riege, T. Pardini, M. M. Seibert, J. Evans, S. Boutet and M. Frank, *Scientific Reports*, 2014, **4**, 6026.
17 N. Coquelle, A. S. Brewster, U. Kapp, A. Shilova, B. Weinhausen, M. Burghammer and J.-P. Colletier, *Acta Crystallogr., Sect. D: Biol. Crystallogr.*, 2015, **71**, 1184–1196.
18 T. D. Murray, A. Y. Lyubimov, C. M. Ogata, H. Vo, M. Uervirojnangkoorn, A. T. Brunger and J. M. Berger, *Acta Crystallogr., Sect. D: Biol. Crystallogr.*, 2015, **71**, 1987–1997.
19 K. Dhouib, C. Khan Malek, W. Pfleging, B. Gauthier-Manuel, R. Duffait, G. Thuillier, R. Ferrigno, L. Jacquamet, J. Ohana, J.-L. Ferrer, A. Théobald-Dietrich, R. Giegé, B. Lorber and C. Sauter, *Lab Chip*, 2009, **9**, 1412–1421.
20 C.-C. Chang, K. W. Kolewe, Y. Li, I. Kosif, B. D. Freeman, K. R. Carter, J. D. Schiffman and T. Emrick, *Adv. Mater. Interfaces*, 2016, **3**, 1500521.
21 G. Pérez-Mitta, J. S. Tuninetti, W. Knoll, C. Trautmann, M. E. Toimil-Molares and O. Azzaroni, *J. Am. Chem. Soc.*, 2015, **137**, 6011–6017.
22 D. E. Acevedo-Cartagena, J. Zhu, E. Trabanino, E. Pentzer, T. Emrick, S. S. Nonnenmann, A. L. Briseno and R. C. Hayward, *ACS Macro Lett.*, 2015, **4**, 483–487.
23 T. Graber, S. Anderson, H. Brewer, Y. S. Chen, H. S. Cho, N. Dashdorj, R. W. Henning, I. Kosheleva, G.

Macha, M. Meron, R. Pahl, Z. Ren, S. Ruan, F. Schotte, V. Srajer, P. J. Viccaro, F. Westferro, P. Anfinrud and K. Moffat, *Journal of Synchrotron Radiation*, 2011, **18**, 658–670.
24 Z. Dauter, *Methods in Enzymology*, 1997, **276**, 326–344.